Engineering Fracture Mechanics 314 (2025) 110713

Contents lists available at ScienceDirect

Engineering Fracture Mechanics

journal homepage: www.elsevier.com/locate/engfracmech

Investigation of microscale brittle fracture opening in diamond with olivine inclusion using XFEM and cohesive zone modeling

Biswabhanu Puhan [a,*], Alessia Patton [b], Simone Morganti [c], Greta Rustioni [d], Alessandro Reali [e], Matteo Alvaro [a]

[a] Department of Earth and Environmental Sciences, University of Pavia, Via A. Ferrata 1,, 27100 Pavia, Italy
[b] Department of Civil Engineering and Environmental sciences, Universität der Bundeswehr München, Werner-Heisenberg-Weg 39, 85577 Neubiberg, Germany
[c] Department of Electrical, Computer, and Biomedical Engineering, University of Pavia, Via A. Ferrata 5, 27100 Pavia, Italy
[d] Bayerisches Geoinstitut, University of Bayreuth, 95440 Bayreuth, Germany
[e] Department of Civil Engineering and Architecture, University of Pavia, Via A. Ferrata 3, 27100 Pavia, Italy

ARTICLE INFO

Keywords:
Host-inclusion systems
Geological applications
Residual Stress Relaxation
Brittle Fracture
Extended Finite Element Method (XFEM)

ABSTRACT

Inclusions trapped in diamonds are a fundamental source of information to probe the Earth's interior, provided that the pressure conditions at which the diamond grew are correctly determined. This study explores the traditional assumptions in geothermobarometry for olivine-in-diamond host-inclusion systems by employing extended finite element methods (XFEM) and cohesive zone models (CZM) to quantify the contributions of brittle fractures to the relaxation of the residual stress of inclusions. Our analysis was performed assuming that the host-inclusion system does not contain fluids and that the unfractured minerals are elastically isotropic. Our models show that the damage initiation is solely dependent on the shape of the inclusion and on the fracture strength of the diamond host, while the fracture nucleation is influenced by both the size of the inclusion and the toughness of the diamond. Our findings indicate that, in dry systems, the amount of relaxation of residual stress of the inclusion due to the opening of brittle fractures is much lower than that due to the elastic interaction between the host and the inclusion. Moreover, the pressure release due to fractures is not substantially affected by the shape of the inclusion. We also show that the total relaxation of the residual pressure due to the combined effect of the elastic interaction and the brittle deformation is lower than what is observed in natural samples, even when assuming fracture strength and toughness lower than those reported from experiments on single crystals of diamond. Such discrepancies suggest that in natural olivine-diamond systems additional mechanisms such as viscous or plastic deformation and/or the presence of preexisting defects and fluids in the host might play a relevant role in the relaxation of the residual stress. These findings underscore the need for advanced numerical tools that consider the complex interplay of the geometry of the host-inclusion system, the fracture properties, and the presence of fluids and defects in order to build more accurate models to constrain the geological history of diamonds.

* Corresponding author.
E-mail address: biswabhanu.puhan01@universitadipavia.it (B. Puhan).

https://doi.org/10.1016/j.engfracmech.2024.110713
Received 13 August 2024; Received in revised form 15 October 2024; Accepted 1 December 2024
Available online 4 December 2024

Nomenclature

Latin Characters

$\boldsymbol{E}$ [Pa]	Young's Modulus
$\boldsymbol{G_{IC}}$, $\boldsymbol{G_{IIC}}$, and $\boldsymbol{G_{IIIC}}$ [J/m^2]	Critical energy release rates for each fracture mode
$\boldsymbol{K_{IC}}$, $\boldsymbol{K_{IIC}}$, and $\boldsymbol{K_{IIIC}}$ [MPa·m$^{0.5}$]	Fracture toughness parameters for each fracture mode
$\boldsymbol{P}$ [Pa]	Pressure
$\boldsymbol{T}$ [K]	Temperature
$\boldsymbol{P_{end}}$ [Pa]	Final pressure after exhumation
$\boldsymbol{T_{end}}$ [K]	Final temperature after exhumation
$\boldsymbol{P_{thermo}}$ [Pa]	Overpressure of the inclusion
$\boldsymbol{P_{trap}}$ [Pa]	Pressure at entrapment conditions
$\boldsymbol{T_{trap}}$ [K]	Temperature at entrapment conditions
$\boldsymbol{V_{host}}(\boldsymbol{P},\boldsymbol{T})$[m^3]	Unit-cell volume of the host mineral at pressure (P) and temperature (T)
$\boldsymbol{P_{inc}}$ [Pa]	Residual inclusion pressure
$\boldsymbol{V_{inc}}(\boldsymbol{P},\boldsymbol{T})$[m^3]	Unit-cell volume of the inclusion mineral at pressure (P) and temperature (T)

Greek Characters

ν[-]	Poisson's Ratio
$\boldsymbol{\sigma}^{thermo}$ [Pa]	Isotropic stress tensor in Voigt's notation representing uniform overpressure within the inclusion
$\boldsymbol{\alpha}$ [-]	Power-law criterion parameter for mixed-mode fracture behavior

Abbreviations and Special Functions

XFEM	eXtended Finite Element Method
CZM	Cohesive Zone Model
TSL	Traction-Separation Law
EoS	Equation of State
$\mathbf{f_{tol}}$	Tolerance for additional crack growth in ABAQUS XFEM
$\mathbf{f^{g}_{tol}}$	Tolerance for existing crack extension in ABAQUS XFEM

1. Introduction

Inclusions trapped in diamonds are a fundamental source of information to probe the Earth's interior at the conditions at which diamonds grew. In order to constrain the complex history of growth and exhumation of diamonds, it is fundamental to determine the pressure (P) and temperature (T) of encapsulation of the inclusion minerals in the diamond host (e.g., [45,51,55]). Entrapment pressures can be obtained in a variety of manners including elastic geothermobarometry, a method that exploits the contrast in elastic properties between the host and inclusion minerals to determine the pressure at which the inclusion has been enclosed in its host (Angel, Alvaro, et al., 2015; [6]; Angel, Nimis, et al., 2015; [13]; Howell et al., 2012; [31,47]). For the case of inclusion in diamonds, when the diamonds are studied at the Earth's surface, the inclusions are typically over-pressurized because the diamond is much stiffer and possesses a lower thermal expansion than all of the silicate minerals found as inclusions. Upon exhumation to ambient conditions, the diamond expands less than the inclusion, and, as a consequence, when the diamond is in the laboratory the inclusion crystal is constrained to have a smaller volume (i.e., higher pressure) than a free crystal of the same mineral would have at room conditions. Elastic geothermobarometry has been applied to various types of inclusions in diamonds [11,12,18,26,29]; Howell, Wood, et al., 2012; [28,30,32,46,56] under the main assumption that the rheology of both the diamond and the inclusion were elastic during the entire exhumation. In the case of inelastic (i.e., plastic, brittle, viscous) deformation of the host after diamond growth and inclusion entrapment, the inclusion's stress may be less than what expected if the behavior was purely elastic. In this case, the pressure of the inclusion is said to be inelastically relaxed, and the amount of pressure relaxation should properly be accounted for in order to correctly estimate the P and T conditions of entrapment. The mechanism that leads to the inelastic relaxation of the inclusion's stress and the magnitude of the relaxation depend on a range of factors including among others the pressure and temperature (i.e., depth) at which the inclusion was entrapped, the velocity of the exhumation process, the presence of fluids [17,48,71]. The traces of brittle and viscous deformation in the diamond host around the inclusion can be detected by a variety of techniques, including X-ray micro-tomography [37,48,54,63] and topography (e.g., [2], and EBSD (e.g., [73]). The residual strain and stress of the inclusions can be determined using X-ray diffraction and, for specific phases, Raman spectroscopy [13]; Howell, Wood, et al., 2012; [28,44]. By combining different techniques, it is therefore possible to determine the residual stress of the inclusion and to find evidence of inelastic processes that could have affected the stress of the inclusion. One example for which the inclusions pressures have been very carefully determined is that of diamonds from Udachnaya mine, for which the residual pressures determined on most of the inclusions are lower than 0.5 GPa (see Fig. 1). This value of residual pressure would correspond to entrapment conditions at pressures and temperatures lower than the diamond stability field if the deformation of the host and the inclusion from entrapment conditions to the Earth's surface were purely elastic. However, some exceptional residual pressure values, such as those from the Changma Kimberlite Belt in China, have been

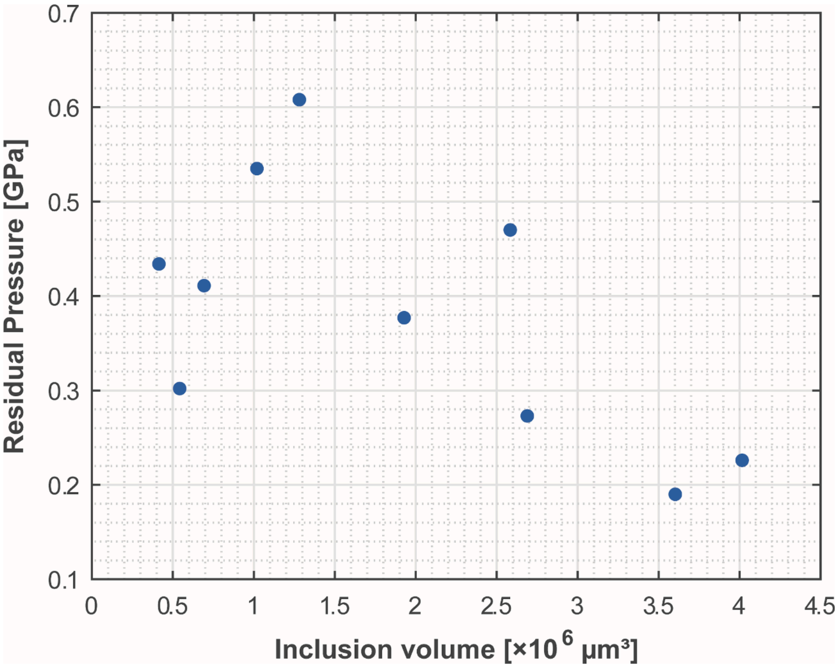

Fig. 1. Pressure of olivine inclusions in diamond hosts from the Udachnaya kimberlite plotted as a function of the inclusion size. The residual pressure was determined through X-ray diffraction and the EoS of Angel et al., 2018 [5]. The Data are from [6,52,53].

recorded to reach as high as 1.4 GPa [61]. This suggests that the entrapment pressures recalculated with purely elastic models are underestimated, pointing to a possible release of the residual pressures of the inclusions due to fractures and/or viscous deformation (e.g., [70]). Previous studies showed that most of the inclusions in these samples are surrounded by fractures which are filled by phases that are likely precipitated from a fluid [6,48,52,53]. As the presence of fractures in diamond-inclusions systems is common, and often leads to the underestimation of the entrapment conditions of these samples, we have investigated the fracture mechanism of the olivine-in-diamond system using numerical modeling. With this approach we can evaluate how fractures develop around olivine inclusions because of the overpressure developed in the inclusion during the exhumation. Our results also allow us to assess the amount of relaxation of the inclusion pressure due to fracture opening, compared to what expected from a purely elastic behavior.

2. Methods

In our simplified model, we split the calculation of the strain and stress of the inclusion into two steps. First, the strain of the inclusion is computed due to the elastic deformation of the cavity of the host diamond from entrapment to the final (P_{end}, T_{end}) conditions. This step assumes that during the fast exhumation of the diamond to the Earth's surface the behavior of the host is mainly elastic, without any viscous relaxation. In the second step, the elastic interaction between the host and the inclusion is accounted for, and the overpressure of the inclusion (i.e., the difference of the inclusion pressure with respect to the external ambient pressure) is calculated. The initiation and propagation of fractures are evaluated as a consequence of the inclusion overpressure. Our calculations assume that both the host and the inclusions have isotropic elasticity and the fracture properties of the diamond host are also isotropic. Moreover, we assume that the system is dry and does not contain any fluid neither around the olivine inclusion nor as fluid inclusions in the diamond host.

Remark 1: Clarification on Terminology (Inclusion vs. Inhomogeneity)

To prevent any misunderstanding, we use the term 'inclusion' in this manuscript to refer to any material embedded within a host matrix, regardless of whether its material properties differ from those of the host. In several scientific communities, an inclusion with properties different from the surrounding matrix might typically be referred to as an 'inhomogeneity.' However, we choose to use the term 'inclusion' consistently throughout to align with geological terminology, recognizing the embedded material as an inclusion even when its properties differ significantly from the host.

2.1. The strain and stress of the inclusion upon exhumation

The strain generated in the inclusion upon exhumation is calculated by assuming that the initial (P_{trap}, T_{trap}) and final (P_{end}, T_{end}) conditions are hydrostatic and known. When the host-diamond is exhumed to the final external pressure and temperature (P_{end}, T_{end}), the inclusion is constrained to the volume of the cavity at these conditions. We assume that the inclusion completely fills the cavity without empty spaces at both entrapment and at every step of the exhumation. As a first approximation, the volume change of the inclusion is imposed by that of the host, as calculated from entrapment to the final conditions [8,39]. By calling $V_{host}(P,T)$ and $V_{inc}(P,T)$ the unit-cell volume the of host and the inclusion, respectively, at a given P and T, the variation of the unit-cell volume of the inclusion is determined as:

$$\frac{V_{host}(P_{trap},T_{trap})}{V_{host}(P_{end},T_{end})}=\frac{V_{inc}(P_{trap},T_{trap})}{V_{inc}(P_{thermo},T_{end})} \tag{1}$$

The volume of the host at entrapment and final conditions are determined from the equation of state (EoS) of diamond reported by [74]. The volume of the olivine inclusion at entrapment conditions is determined from the volume EoS of Angel et al. [5]. The $V_{inc}(P_{thermo},T_{end})$ is obtained from Eq. (1), and represents the unit-cell volume of the confined inclusion when the host is at room conditions (P_{end},T_{end}). The corresponding pressure P_{thermo} can be determined by the equation of state (EoS) of the inclusion at the volume $V_{inc}(P_{thermo},T_{end})$ and temperature T_{end}.

Once the value of P_{thermo} of the inclusion is obtained from the equation of state, the components of the corresponding isotropic stress tensor (in Voigt's notation; [60]) are obtained as:

$$\sigma^{thermo}=[P_{thermo}\ P_{thermo}\ P_{thermo}\ 0\ 0\ 0]^{T} \tag{2}$$

This is a virtual stress state, which does not satisfy the mechanical equilibrium between the host and the inclusion mineral. The interaction between the host and the inclusion must be accounted for in order to obtain the final configuration of the system at mechanical equilibrium, and therefore the final stress and strain of the inclusion. Most models for Raman thermobarometry assume that the rheology is purely elastic, and therefore implement various elastic formulations of the inclusion problem to solve for the interaction between the host and the inclusion, depending if isotropic or anisotropic properties are used (e.g., [9,7,25,39,42,43,66,68]). In our model, we evaluate two scenarios of interaction. In the first one, the interaction is assumed to be purely elastic, whereas in the second scenario, a fracture criterion is implemented in order to evaluate the final pressure of the inclusion due to fracture initiation and propagation.

2.2. The host-inclusion interaction

The mechanical interaction between the host and the inclusion is evaluated by means of the Finite Element Method (FEM) using the software ABAQUS/CAE version 2020 (Dassault Systèmes Simulia [19]). To this aim, we developed several 3D finite element (FE) geometrical models in which spheroidal inclusions with various aspect ratios are included in a host with cubic shape (see Fig. 2(a)). In order to avoid the effects of pressure on the inclusion due to its proximity to the host surface and to make the analysis insensitive to the shape of the host, the ratio between the longest axis of the inclusion and the side of the host is always maintained at or below 1/25 for all models [38,69]. Without loss of generality, in our analyses, we exploited the symmetry arising from the chosen geometry, isotropic elastic properties, as well as the loading and boundary conditions. Because of this choice, only 1/8 of the entire 3D system is modeled and analyzed (see Fig. 2).

At the beginning of each FE analysis, the stress obtained from Eq. (2) is applied as a prestress to the inclusion, while a hydrostatic stress is applied to the external surfaces of the host and taken equal to the ambient pressure (namely equal to 10^5 Pa). As a

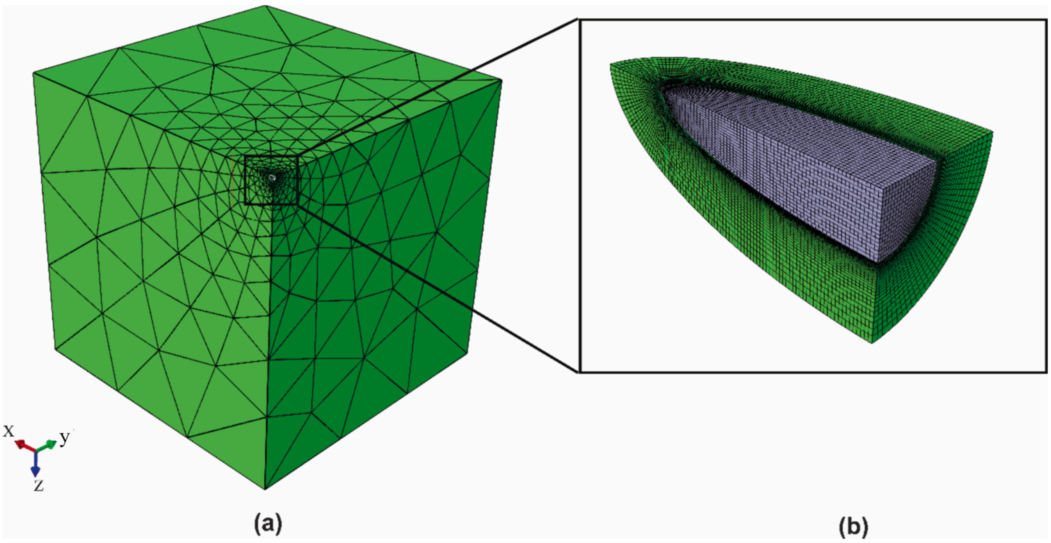

Fig. 2. Example of a geometrical model for the finite element analysis. In this example, the inclusion aspect ratio is 4:1:1, with a ratio between the longest length of the inclusion and the side of the host equal to 1/50. Because of the symmetry of the system, the model reproduces 1/8 of the host-inclusion system (a). The Inclusion (see detail (b) in gray) is surrounded by the mesh enrichment (in green) for the XFEM analysis.

consequence, the host-inclusion system is initially in a non-equilibrated configuration, since the tractions at the host-inclusion interface are not balanced. Suitable Dirichlet boundary conditions are applied to the host to prevent rigid body motions, and the purely elastic interaction is evaluated with FEM assuming linear elasticity with the elastic properties (i.e., Poisson's ratio and Young's modulus) reported in Table 1.

The final residual stress and strain of the inclusion are the results of each finite element analysis. Since the inclusions are ellipsoidal and linear elasticity is assumed, the solutions from the FE analyses were compared to the strain and stress obtained from the analytical solution of Eshelby [21] for the same configuration, obtaining a maximum difference on the average pressure of the inclusion of less than 0.01 % across all models. This allows us to check the elastic solution and perform a mesh convergence analysis in the elastic regime. In the finite element model, the regions with high stress concentrations and significant geometric distortions were carefully refined. These include the inclusion itself and its surrounding areas (considering an offset from the inclusion having a length approximately equal to twice its semiminor axis), which are critical for fracture propagation, as indicated in Fig. 2. For these areas, we employed C3D8I elements from the ABAQUS element library, i.e., 8-node linear brick elements with incompatible modes. These elements were specifically chosen for their superior ability to handle complex stress states and effectively mitigate mesh distortion. Conversely, for the broader areas of the host material where a detailed stress analysis was less critical, we utilized 10-node quadratic tetrahedral elements (C3D10) from the Abaqus element library. This choice was made to optimize computational efficiency while still ensuring accurate results across regions that are less relevant for fracture propagation. The final chosen mesh information, comprising the type and total number of elements, according to the different critical (namely, the inclusion and its surrounding areas) or non-critical regions (i.e., the host far away from the inclusion) for different olivine shapes are summarized in Table 2.

To study crack initiation, propagation, and their consequent impact on the stress and strain in the inclusions, we employed the eXtended Finite Element Method (XFEM)[41]. In XFEM, aside from standard shape functions, enrichment functions are incorporated to model discontinuities such as cracks, based on the partition of unity [40]. In addition to XFEM, we utilize the Cohesive Zone Model (CZM), which provides a phenomenological description of discrete fracture as a material separation across a surface, namely describing the material behavior in the fracture process zone using traction-separation laws (TSL) [14]. Within the CZM, the creation of a new fracture surface is accomplished by allowing initially coherent element boundaries to open according to a cohesive law that models a gradual loss of strength with an increasing separation. The cohesive law determines the work of separation, or fracture energy, required for the complete formation of a free surface [15]. In order to identify the locations of crack nucleation and propagation, we adopt the Rankine criterion that is widely adopted in modeling both brittle and quasi-brittle materials [65]. According to this criterion, either a new crack emerges or a pre-existing crack extends when the maximum principal stress at an integration point exceeds the material's failure strength threshold. In our analyses, the crack propagation direction lies orthogonal to the maximum principal stress direction (Dassault Systèmes Simulia [19,62]). This approach is often favored over other approaches like the maximum circumferential tensile stress criterion, largely because of its capacity for nonlocal calculations, providing a more generalized and robust solution [59,65].

Before the fracture initiation, the behaviour of the material is linear elastic. Then, the onset of fracture leads to a softening behaviour in the material and to a degradation of the stiffness. To model the post-peak softening behavior, a linear TSL within ABAQUS is adopted. After reaching its peak, the traction decreases linearly until a material achieves a critical separation displacement, at which point the traction becomes zero [15].

The inherent softening of the material after the fracture initiation may lead to issues in numerical convergence (Dassault Systèmes Simulia [19,20]). In order to enhance convergence, we adopt a viscous regularization approach [34], such that the tangent stiffness matrix of the softening material remains positive for sufficiently small-time increments. A small value of the viscosity parameter equal to 10^{-4} Pa·s is used within the viscous regularization, in order to improve the convergence without affecting the results. To this aim, we ensured that the energy dissipated due to this regularization remained below 5 % of the model's internal energy, thereby preserving the physical meaning of our results. Further details on the evaluation of the parameters and outcome of viscous regularization in our models are reported in Appendix A.

The fracture toughness determines a material's resistance to crack propagation and is represented by the parameters K_{IC}, K_{IIC}, and K_{IIIC} for the normal, shear, and tangential modes, respectively. Since limited data are available on the shear and tangential modes of single-crystal diamonds, drawing insights from Zhang et al., [67], we assume that $K_{IC} = K_{IIC} = K_{IIIC}$. This simplifying assumption, aligned with diamond's isotropic nature, facilitates our analysis by maintaining uniform fracture toughness across all modes.

Critical energy release rates G_{IC}, G_{IIC}, and G_{IIIC} for each mode are calculated using the relation $G_{ic} = \frac{K_{ic}}{E}$ (with i={I, II, III}), where K_{ic} represents the respective mode's fracture toughness, and E is the Young's modulus. Although the relation for G_{IIIC} could theoretically include adjustments for the material's Poisson's ratio, given diamond's low Poisson's ratio ($\nu = 0.0724$), its effect on G_{IIIC} is minimal. Therefore, for simplification and to ensure consistency in our computational model, we used $G_{IC} = G_{IIC} = G_{IIIC}$.

Thus, the mixed-mode fracture behavior is characterized by the power-law criterion:

Table 1
Elastic properties of host and inclusion minerals.

Mineral Type	Young's Modulus [GPa]	Poisson's Ratio [-]
Diamond	$1.14 \cdot 10^3$	0.0724
Olivine	$1.90 \cdot 10^2$	0.2499

Table 2
Type and total number of elements (to model the host, the inclusion, and the enrichment area around the inclusion) considered to build the Finite Element Abaqus solution for inclusion aspect ratios of 4:1:1 and 10:1:1.

Benchmark	# C3D10 elements in the Host	# C3D8I elements in the enrichment around the Inclusion	# C3D8I elements in the Inclusion
4:1:1	29,276	250,104	58,792
10:1:1	21,860	142,080	38,208

$$\left(\frac{G_I}{G_{IC}}\right)^{\alpha} + \left(\frac{G_{II}}{G_{IIC}}\right)^{\alpha} + \left(\frac{G_{III}}{G_{IIIC}}\right)^{\alpha} = 1 \tag{3}$$

with $\alpha = 1$, indicating that all fracture modes equally influence the damage process in the diamond [3]. This approach aligns with the isotropic fracture behaviour of the material.

3. Results

Soft inclusions in a stiff host develop a pressure higher than the external pressure during the exhumation from the entrapment conditions at crustal or mantle conditions to the Earth's surface. We assumed that the olivine inclusions were entrapped in their diamond host at pressure and temperature conditions equal to 5.5 GPa and 1473.15 K, respectively, a typical average condition for olivine inclusions in diamonds from the Udachnaya kimberlite [1,46]. Our elastic calculations show that the maximum overpressure (defined as the difference between the inclusion pressure and the external ambient pressure acting on the diamond host) developed by the olivine inclusions exhumed to ambient conditions is 1 GPa, and, therefore, we used this value as the highest limit of inclusion overpressure in our models.

3.1. *Damage initiation and fracture nucleation: Shape and size effects of inclusions*

Our investigation delved into the influence of the inclusion shape and size on damage initiation and fracture nucleation. In this study, damage initiation refers to the point when the damage variable (D) in XFEM (referred to as STATUSXFEM in ABAQUS) becomes greater than 0 but less than 1 ($0 < D < 1$), indicating that the material is experiencing microcracking or inelastic deformation, as shown in Fig. 3(b). Fracture nucleation occurs when the damage variable reaches a value of 1, meaning the material is fully fractured and lost its load-bearing capacity, as depicted in Fig. 3(c). We subsequently explored both the impact of the inclusion size and shape on damage initiation.

Fig. 4 clearly shows that, for three distinct inclusion sizes with constant aspect ratios (here both the 4:1:1 and the 10:1:1 scenarios, with dimensions chosen to ensure equal volumes for different shapes, were investigated), a consistent critical fracture strength is required for damage initiation. Above this strength threshold, no damage occurs. This observation underscores the independence of damage initiation from the size of the inclusion. This observation aligns with the findings of Tanné et al., [58], who conducted a damage initiation study for an elliptical hole in an infinite domain subjected to far-field loading. Additionally, we observed that, for damage initiation, the critical fracture strength is entirely independent of fracture toughness, as showcased in Fig. 4.

In Figs. 4 to 7, the precision of the critical fracture strength, overpressure, and fracture toughness values was determined manually. We incrementally adjusted these parameters in steps of 0.001 GPa (or 0.008 MPa·m$^{0.5}$ for fracture toughness) and observed when either damage initiation or fracture nucleation occurred. A negative precision value indicates that the parameter was increased from

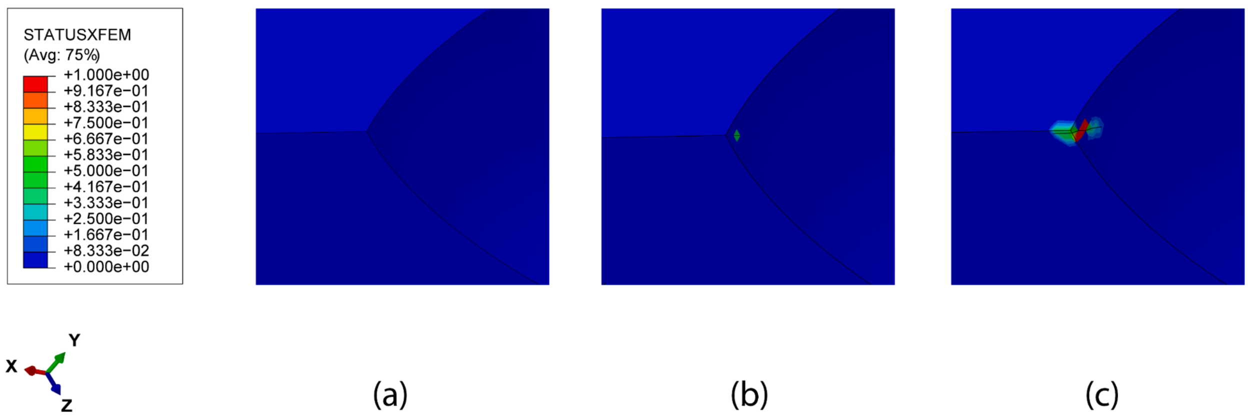

Fig. 3. Stages of fracture development in the host material (diamond): (a) Elastic phase with no damage ($D = 0$), (b) Onset of initial damage ($0 < D < 1$), (c) Nucleation of the first fracture ($D = 1$). The processes of damage initiation and fracture nucleation are illustrated at the tip of the inclusion within the host.

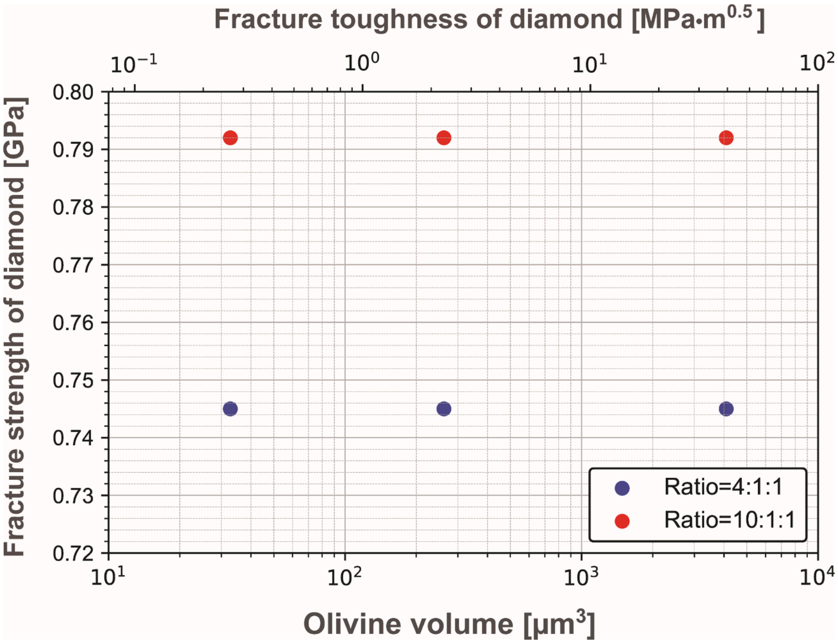

Fig. 4. Fracture strength needed for the damage initiation (0 < D < 1), for ellipsoidal inclusion of aspect ratios 4:1:1 and 10:1:1 with respect to different inclusion sizes and fracture toughness, for the inclusion overpressure $P_{thermo} = 1$ GPa. The results highlight that the damage initiation simply depends on the shape of the inclusion and is independent of fracture toughness and inclusion size. The critical fracture strength is the value above which no damage can initiate and is approximately 0.745 GPa and 0.792GPa for 4:1:1 and 10:1:1 shapes, respectively (with a precision of + 0.001 GPa).

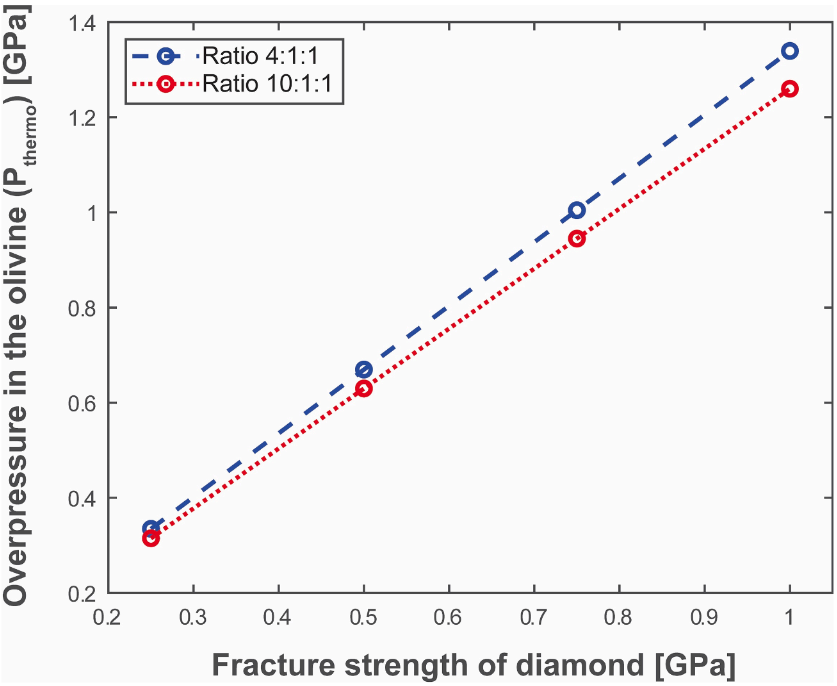

Fig. 5. Relation between the minimum overpressure in the inclusion for damage initiation (0 < D < 1), and the fracture strength for ellipsoidal inclusions with aspect ratios of 4:1:1 and 10:1:1. A linear dependence of the minimum overpressure on the fracture strength is found for each considered aspect ratio. The lines identify the critical overpressure corresponding to the fracture strength above which no damage can initiate (with a precision of + 0.001 GPa).

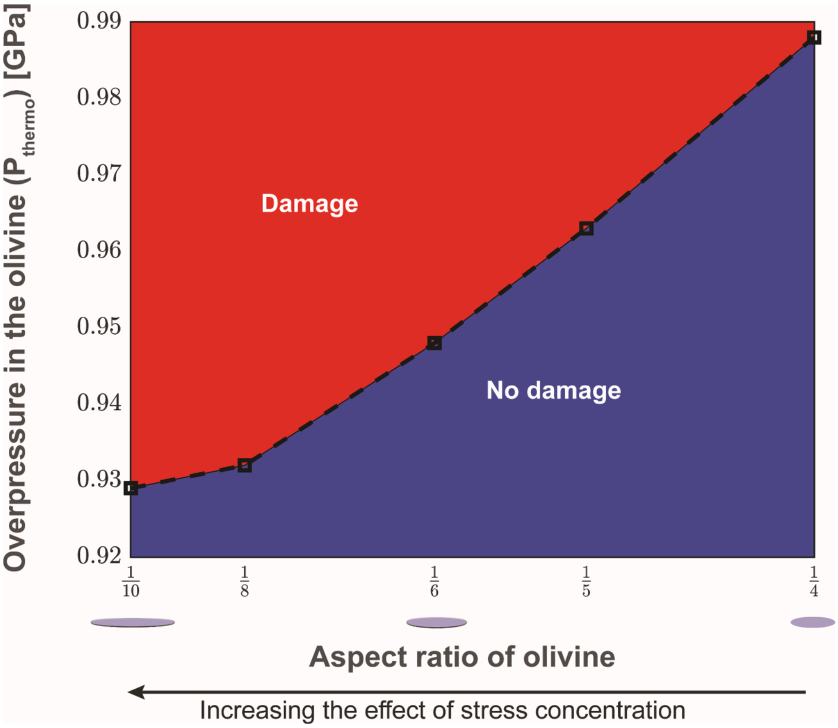

Fig. 6. Overpressure in the inclusion required to induce the first damage ($0 < D < 1$), in host for different aspect ratios, given a fracture strength of 0.738 GPa. Aspect ratios are represented using the major axis as the denominator (e.g., 4:1:1 becomes 1/4). This analysis is independent of the size of the inclusion and of the diamond toughness, as detailed in Fig. 4. The critical overpressure is the value below which no damage can initiate (represented by black dashed lines with a precision of −0.001 GPa, indicating that the critical overpressure was determined by increasing the overpressure from lower values until damage initiated). The black squares along the dashed line represent the results of XFEM simulations.

lower values until damage initiation occurred, while a positive precision value indicates that the parameter was decreased from higher values until either damage initiation or fracture nucleation occurred, depending on the specific context.

We also explored the minimum overpressure of the inclusion needed for damage initiation in elongated ellipsoidal inclusions with two aspect ratios (i.e., 4:1:1 and 10:1:1) by varying the fracture strength (see Fig. 5). A constant fracture toughness is adopted for the diamond (namely, equal to 0.1 MPa·$m^{0.5}$). However, the results of Fig. 5 are not affected by this specific choice since the initiation of damage is controlled exclusively by the fracture strength of the material. Fig. 5 shows that the minimum overpressure required to initiate damage in the diamond host around the olivine inclusion linearly depends on the magnitude of the fracture strength of the diamond host. For all values of fracture strength, more overpressure is required to initiate damage around the inclusion with an aspect ratio of 4:1:1. This indicates that the stress concentration at the tip of the inclusion, which increases with its aspect ratio, plays a key role in controlling the damage initiation. Furthermore, we observe that for low values of fracture strength, the curves in Fig. 5 converge, meaning that the overpressure required to initiate damage becomes independent of the aspect ratio of the inclusion. For high fracture strength values, a lower overpressure is required to initiate damage around the inclusion with an aspect ratio of 10:1:1.

Assuming a maximum inclusion overpressure of 1 GPa for the host-inclusion system exhumed to room conditions, our observations suggest that a fracture strength of approximately 0.745 GPa is needed for damage initiation in an ellipsoidal inclusion with an aspect ratio of 4:1:1 (as discussed in Fig. 4). However, to capture resolvable fracture propagation, we adopted a slightly lower fracture strength of 0.738 GPa. This value was chosen to ensure consistent observation and analysis of fracture propagation in all subsequent models, particularly when examining the effects of inclusion shape and size after fracture propagation.

With the fracture strength set at 0.738 GPa, we then investigated how the aspect ratios affect the required overpressure for damage initiation, as depicted in Fig. 6. We identified a critical overpressure threshold; damage initiation only occurs above this threshold for the specified fracture strength. Due to high stress concentrations at the tips of prolate inclusions, the critical overpressure decreases as the aspect ratio increases. This analysis focuses solely on the initiation of damage, as previously explained, and is independent on the size of the inclusion and the toughness of the diamond.

Then, we turned our attention to understanding parameters affecting fracture nucleation. In our investigations, we maintain a constant fracture strength of 0.738 GPa. By systematically varying the size of the inclusion, we plotted the critical fracture toughness required for the nucleation of the first fracture, as illustrated in Fig. 7.

Fig. 7 reveals that fracture toughness significantly affects fracture nucleation, showing a linear scaling of the critical fracture toughness with the power 1/6 of the inclusion volume. Critical fracture toughness is established as the threshold value: brittle fractures will nucleate at or below this level, but not above it, for a given fracture strength. The dashed black line represents an extrapolation for

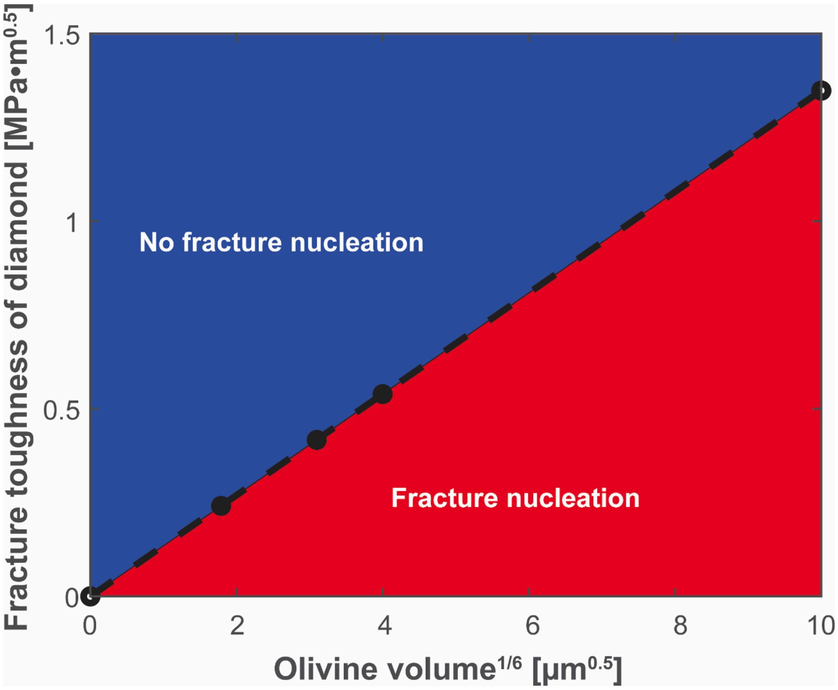

Fig. 7. Dependency of the fracture toughness for nucleating the first fracture (Damage variable D = 1) on the inclusion volume raised to 1/6 power. The critical fracture toughness, denoted by a black dashed line with a precision of + 0.008 MPa·m$^{0.5}$, is defined such that fracture will not nucleate above it. The ellipsoidal inclusion in this example has a 10:1:1 aspect ratio and a constant fracture strength of 0.738 GPa, and the inclusion overpressure is assumed to be 1 GPa. The black circles along the dashed line represent the results of XFEM simulations. The dashed line fits the results of our XFEM simulations and shows that a scaling exists between the critical fracture toughness and the inclusion volume. Such relationship allows the extrapolation of the critical fracture toughness to the volume range of typical natural inclusions in diamond that are larger than 0.5·10^{6} μm^{3}.

the actual volume of natural inclusions, typically larger than 10^{6} μm^{3}. This extrapolation suggests that the critical fracture toughness of the diamond surrounding natural inclusions with a volume of 10^{6} μm^{3} is approximately 1.35 MPa·m$^{0.5}$.

3.2. *The influence on residual inclusion pressure (P_{inc}) due to the shape of the inclusions*

We selected a fracture strength of 0.738 GPa and a low fracture toughness of 0.1 MPa·m$^{0.5}$ for our subsequent studies on fracture propagation in order to ensure the occurrence of brittle fractures–characterized by high fracture strength and low toughness. This choice aims to precisely study how these properties influence the mechanics of brittle fracturing, particularly in the context of different inclusion geometries.

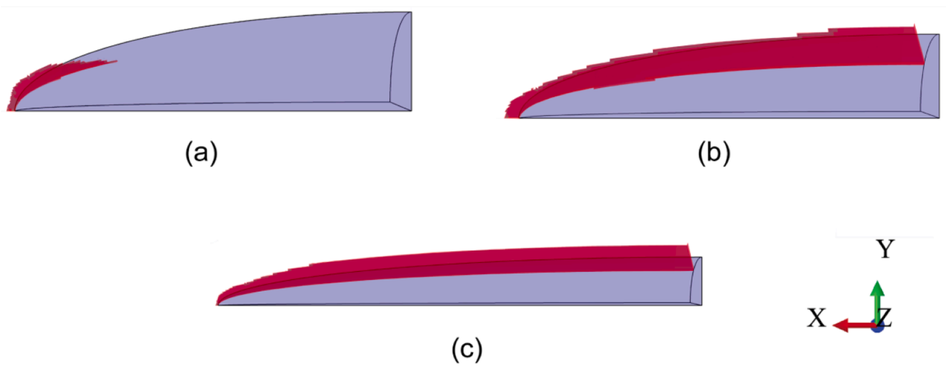

Fig. 8. Visualization of fracture propagation (in red color) in diamond hosts due to over-pressurized inclusions with increasing aspect ratios: (a) 4:1:1, (b) 5:1:1, (c) 10:1:1. Analyses conducted with a fracture strength of 0.738 GPa and a fracture toughness of 0.1 MPa·m$^{0.5}$. All inclusions maintain a constant volume of approximately 4090 μm^{3} across different shapes. Note that only 1/8 of the inclusion is represented in each case.

The extent of the fractures developed around the inclusion is a consequence of the stress concentration and increases with the aspect ratio (see Fig. 8). As shown in Fig. 9, the extent of the fractures is tightly related to the amount of the inclusion pressure that is relaxed as a result of fracturing. Inclusions with an aspect ratio of 3:1:1 or less show an average residual pressure identical to that expected assuming a purely elastic behaviour, implying no significant relaxation due to fractures. The effect of fractures becomes resolvable for the 4:1:1 aspect ratio (Fig. 9). The relaxation of pressure due to fractures further increases for inclusions with larger aspect ratios. However, inclusions that are more elongated (up to an extreme aspect ratio of 10:1:1) do not experience a significantly larger relaxation of pressure.

Fig. 10 showcases the stress distribution for two distinct geometric configurations: 4:1:1 and 10:1:1. In their initial elastic analysis phases (depicted in subfigures (a) and (c)), both configurations exhibit a uniform stress distribution. However, the 10:1:1 shape inherently has a more relaxed profile as compared to the 4:1:1 shape. As fractures develop, as seen in Fig. 10 (b) and (d), this uniformity is lost. The 4:1:1 shape begins to display a non-uniform stress distribution because of the appearance of small fractures, whereas the 10:1:1 shape, which induces the growth of a larger fracture, exhibits a more pronounced deviation from uniform stress. This delineates the transformative effect of fractures on stress distribution within the inclusion.

3.3. *The influence on residual inclusion pressure (P_{inc}) due to the size of the inclusion*

Simulations were conducted to assess the impact of the size of the inclusion on the residual inclusion pressure (P_{inc}). The diamond host has a failure strength of 0.738 GPa and a fracture toughness of 0.1 MPa·m$^{0.5}$, while the aspect ratio of the inclusions is fixed to 10:1:1. The numerical results reported in Fig. 11 show a distinct relationship between the volume of the inclusion and the residual inclusion pressure (P_{inc}). As the inclusion size increases, P_{inc} initially decreases because of the fracture propagation driven by the stress concentrations at the tip of the inclusion. However, with the current choice of fracture parameters, P_{inc} becomes independent on the inclusion size for inclusions having a volume larger than 33 μm^3. This shows that, as the inclusion size increases, the system approaches a critical state where the available mechanical energy for crack propagation is fully utilized. Beyond this point, the material's inherent toughness and strength prevent further effective stress redistribution, limiting fracture propagation. Consequently, the residual inclusion pressure remains constant, reflecting that additional increases in inclusion size do not yield further stress intensification or fracture propagation due to the saturation of energy absorption capacity in the material[4]. The behaviour summarized in Fig. 11 is also observed for natural fluid inclusions entrapped in mineral phases. Measurements of fluid inclusions in quartz with a wide range of sizes show that the internal pressure is higher in small inclusions and reaches a constant value for large inclusions (e.g., Fig. 3 in [16]).

4. Discussion and implications

The determination of the pressure of entrapment of mineral inclusions in diamonds is fundamental in order to constrain the geological history of diamonds. Current models assume that the diamond host and its inclusions behave purely elastically during the fast exhumation from the Earth's mantle to the ambient conditions at the Earth's surface where diamonds are found. However, this assumption is challenged by the fact that measurements on natural diamonds often reveal extensive brittle deformation around the minerals inclusions contained in them, such as olivines, which are often surrounded by fluid rims [48]. Moreover, the measured residual pressure of such inclusions is too low to be explained by simple elastic models, as the recalculated entrapment conditions would place the diamond growth at pressures lower than the geological window of diamond formation [55]. Even elastic models that include the effect due to the presence of a fluid rim around the inclusion cannot explain the reduced residual pressure observed in natural olivine inclusions, as the additional contribution arising from the opening of fractures is not accounted for [10]. Therefore, a comprehensive understanding of the brittle fracture mechanisms around inclusions in diamonds is required in order to develop more accurate models of geobarometry. To this end, simulation modeling provides a straightforward way to test and explore different "what-if" scenarios. Namely, our models to delve into fracture openings in host-inclusion systems consider a combination of XFEM and CZM and our numerical results explore the effects of brittle fractures on damage initiation, fracture nucleation and propagation, with a particular emphasis on the roles of inclusion shape, size and fracture properties of diamond.

Our findings reveal that:

- Damage initiation is found to be independent of the inclusion's size and fracture toughness of the diamond, depending solely on the inclusion's shape and the diamond's fracture strength. Subsequently, once damage initiates, fracture nucleation becomes dependent on both the inclusion's size and fracture toughness of the diamond.
- Critical values of fracture strength and toughness exist for propagation of fractures around olivine inclusions in diamond. In particular for a diamond's fracture strength above 0.8 GPa and fracture toughness above 1.35 MPa·m$^{0.5}$ (for inclusions with volume $> 10^6$ μm^3), no fracture nucleation is observed for the typical overpressure of olivine inclusions. The former is determined to be independent of inclusion's size, while the toughness exhibits a dependency on size, with a linear relationship with the power 1/6 of the volume.

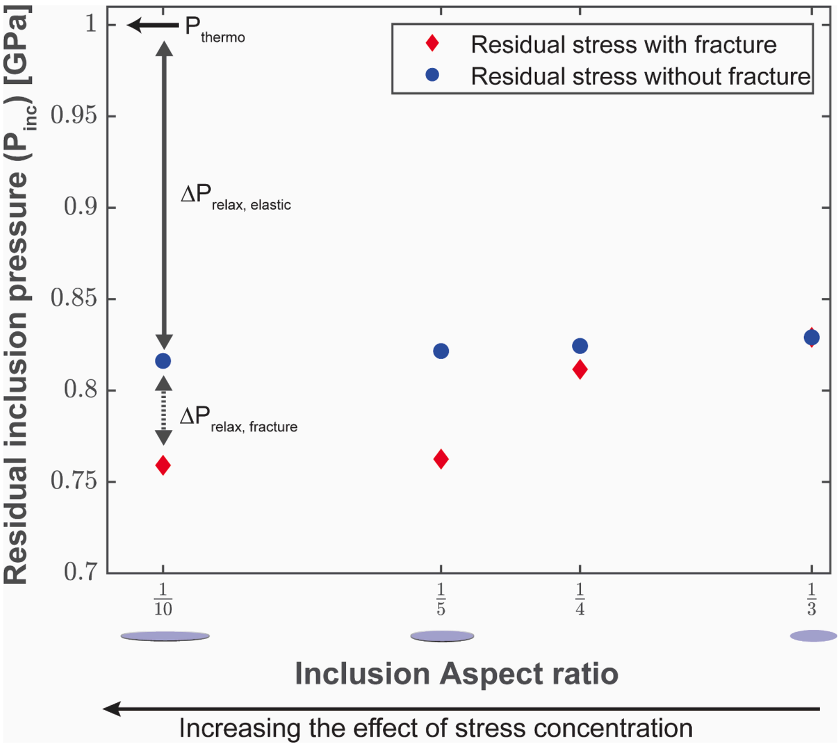

Fig. 9. Relaxed pressure of the inclusion after the fracture opening as a function of the normalized aspect ratio of the inclusion. The latter is represented with the major axis as the denominator (e.g., aspect ratio 4:1:1 becomes 1/4). All these analyses are done by considering fracture strength = 0.738 GPa and fracture toughness = 0.1 MPa·m$^{0.5}$. A volume of approximately 4090 μm^3 is assumed for all shapes. The relaxed pressure corresponds to the residual inclusion pressure (P_{inc}), calculated as the average pressure across all elements at the end of the simulation.

- Furthermore, our investigation reveals that when considering only the effect of inclusion's shape, the relaxation of inclusion residual pressure due to brittle fractures is relatively low, approximately 5–6 % of the inclusion overpressure (P_{thermo}), bringing the residual pressure to about 0.76 GPa for an entrapment pressure–temperature conditions of 5.5 GPa and 1473.15 K. Moreover, our analysis highlights that the damage initiation is significantly influenced by the stress concentration induced by the aspect ratio of the inclusion. However, while the initial increase in aspect ratio significantly impacts fracture propagation, this effect diminishes for inclusions with extreme aspect ratios, such as 10:1:1. As a result, prolate inclusions with extreme aspect ratios do not experience a significantly larger relaxation of the residual pressure (see Fig. 9).

Despite showing that the opening of fractures in diamond around olivine inclusions affects the relaxation of the inclusion pressure, the models herein presented do not fully explain the observations obtained from natural olivine inclusions in diamonds (Fig. 1). Measurements of natural samples show that the residual pressure of fractured olivine inclusions in diamond is often below 0.5 GPa [6,52]. A residual pressure of 0.5 GPa is considered a threshold value, as any pressure lower than this value would not be compatible with an entrapment in the diamond stability field, unless an inelastic process relaxes the pressure of the inclusion during the exhumation [6]. The observation of olivine inclusions with a residual pressure below this threshold (see Fig. 1) suggests that a higher degree of relaxation occurs in natural samples than our models predict. Moreover, fractures are also observed around olivine inclusions with an aspect ratio lower than 4:1:1, despite the fracture properties implemented in our model being significantly lower than the strength of 4 GPa and fracture toughness of 5–16 MPa m$^{0.5}$, reported for natural single crystal diamonds [22,27,35].

The lower residual pressure observed in natural inclusions might be due to other factors not included in our model, such as viscous relaxation. However, the quick ascent of the kimberlite magma that brings the diamonds from mantle depths to the Earth's surface conditions limits the amount of viscous relaxation [70]. Moreover, the viscous relaxation of the diamond host would reduce the inclusion overpressure, therefore limiting the nucleation of fractures, a behavior that would not agree with the observation of extended fracture networks around natural olivine inclusions. Additionally, the exhumation rate may influence the brittle/ductile behavior of diamonds. High strain rates during exhumation, as highlighted by Luisier et al., [36], can promote earlier fracture initiation due to induced brittle behavior, explaining the early fractures observed in natural samples. Furthermore, real inclusions often have edges or corners, unlike the ellipsoidal point singularities modeled in our simulations. These corners induce stress concentrations which could lead to earlier fracture initiation, a factor not captured by our models but observed in natural samples [64]. Fracture strength is known to decrease with the presence of defects and impurities, and it inversely correlates with the presence of pre-existing fractures [22].

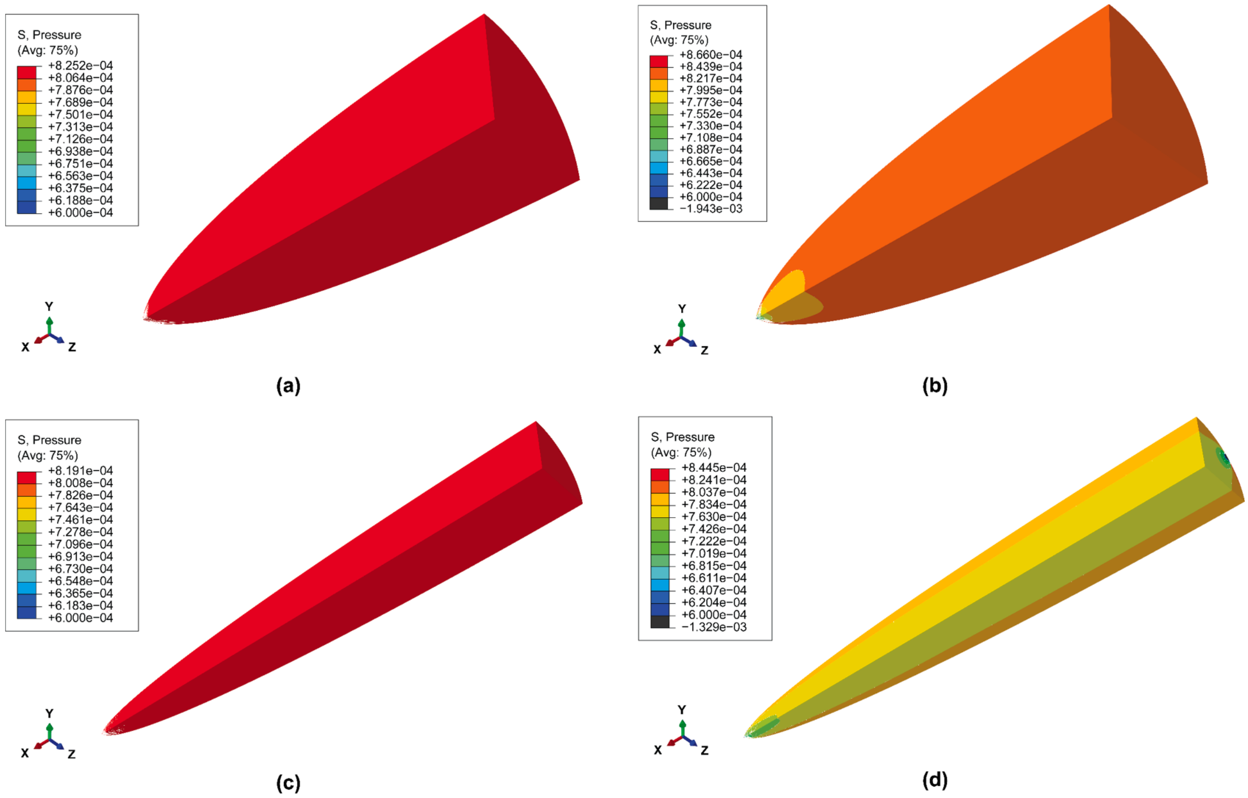

Fig. 10. Distribution of the residual pressure [N/μm^2] in olivine inclusions assessed for an exhumation of the olivine-diamond system from entrapment conditions (P, T) = (5.5 GPa, 1473.15 K) to ambient conditions: (a) Residual pressure of an inclusion with aspect ratio 4:1:1 evaluated with a purely elastic model. (b) Residual pressure of the 4:1:1 inclusion after the opening of fractures. (c) and (d) are analogous to Fig. (a) and (b), respectively, and are calculated for an inclusion with aspect ratio 10:1:1. The pressure distribution in the inclusion is homogeneous for purely elastic deformations, while it becomes non-homogeneous when fractures are developed. As discussed above, because of symmetry, 1/8 of the inclusion is representative of the entire system. All these analyses are performed with a fracture strength of 0.738 GPa and fracture toughness of 0.1 MPa·m$^{0.5}$. A volume of approximately 4090 μm^3 is assumed for all shapes.

Similar to this, the strength of a material is reduced by the presence of inclusions [4,23] and the toughness is reduced due to their size and distribution [50,57,72]. Our simulations show that the magnitude of the critical fracture toughness, which quantifies the highest value of toughness of the diamond host that still permits the opening of cracks, given a specific volume of the inclusion, increases as a function of the volume of the inclusion (see Fig. 7). On the other hand, experimental studies found that the fracture toughness of a material decreases with increasing inclusion size [50,72]. Therefore, a natural diamond containing olivine inclusions has a lower fracture toughness than a perfect single crystal of diamond would have, and a critical threshold size of the inclusion, for which the toughness of the host diamond falls below the critical toughness necessary to open fractures around that inclusion, may exist. Such behaviour would explain the decrease of fractures intensity with inclusion size observed for olivine inclusions in diamonds by Synchrotron Radiation X-ray Tomographic Microscopy investigations [53]. A similar dependency is commonly observed also for fluid inclusions in metamorphic rocks, for which a threshold size for the decrepitation of the inclusion is observed (e.g., [16]. Moreover, fluid rims are typically observed surrounding olivine inclusions in diamonds [48]. The presence of fluids can decrease the fracture strength of the diamond host [24,33], therefore promoting the fracture nucleation. Lower values of fracture strength and toughness would require less overpressure of the inclusion and less stress concentration to trigger the fracturing. Therefore, fracture could nucleate around inclusions with low aspect ratios and whose pressure is partially viscously relaxed, leading to a lower residual pressure of the inclusion compared to that predicted in the current models. These findings underscore the need for advanced numerical tools that consider the complex interplay of the geometry of the host-inclusion system, anisotropic material properties of host and inclusion, the fracture properties of host, and the presence of fluids and defects in order to build more accurate models to constrain the geological history of diamonds.

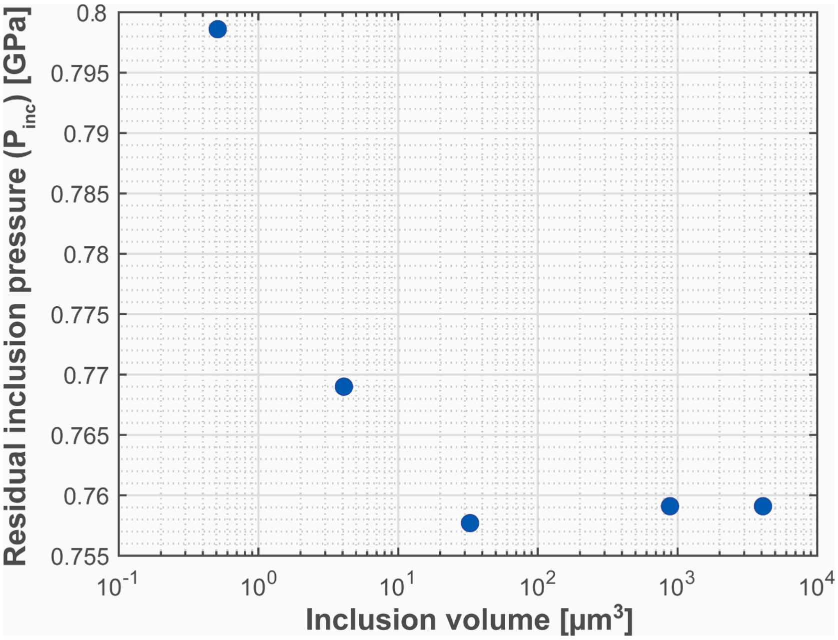

Fig. 11. Residual inclusion pressure as a function of the inclusion volume. Our simulations indicate that as the inclusion volume increases, there is an initial decrease in P_{inc}, which stabilizes at larger volumes, exhibiting a plateau starting from approximately 33 μm^3. The analysis has been done for an aspect ratio of 10:1:1, a failure strength of 0.738 GPa, and a toughness of 0.1 MPa·m$^{0.5}$. The residual inclusion pressure (P_{inc}) is calculated as the average pressure across all elements at the end of the simulation.

CRediT authorship contribution statement

Biswabhanu Puhan: Writing – review & editing, Writing – original draft, Software, Methodology, Investigation, Formal analysis, Conceptualization. **Alessia Patton:** Writing – review & editing, Supervision, Conceptualization. **Simone Morganti:** Writing – review & editing, Supervision. **Greta Rustioni:** Writing – review & editing, Supervision. **Alessandro Reali:** Writing – review & editing, Supervision, Conceptualization. **Matteo Alvaro:** Writing – review & editing, Supervision, Project administration, Conceptualization.

Declaration of competing interest

The authors declare the following financial interests/personal relationships which may be considered as potential competing interests: Matteo Alvaro reports financial support was provided by Ministry of Education and Merit. If there are other authors, they declare that they have no known competing financial interests or personal relationships that could have appeared to influence the work reported in this paper.

Acknowledgments

This work was financially supported by the Fondazione Cariplo (grant agreement #2023-2431 to M. Alvaro), the PRIN-MIUR project (grant no. 2020WPMFE9 to G. Pennacchioni), and the PRIN-MIUR project (grant no. 2022AL5MSN to M. Cremonesi). Additionally, we acknowledge Banca Intesa for funding Biswabhanu Puhan's PhD. A. Reali acknowledges the contribution of the National Recovery and Resilience Plan, Mission 4 Component 2 – Investment 1.4 – CN_00000013 "CENTRO NAZIONALE HPC, BIG DATA E QUANTUM COMPUTING," spoke 6, as well as the support of the Italian Ministry of University and Research (MUR) through the PRIN project COSMIC (No. 2022A79M75), funded by the European Union - Next Generation EU.

Appendix A. Sensitivity studies to different numerical parameters: tolerances, pseudo-time step size, and viscosity coefficient

In this appendix, a comprehensive sensitivity analysis for the numerical parameters needed to utilize XFEM within ABAQUS/CAE for the fracture simulations of the host-inclusion system is reported. The parameters under investigation include the pseudo-time step size, viscosity coefficient, and tolerances for damage initiation and fracture propagation.

Effect of tolerances

Tolerances have particular importance due to their potential influence on the simulation outcomes. Functioning as a pivotal feature within ABAQUS XFEM, tolerance parameters determine the numerical level of acceptance such that an additional crack is introduced, or the length of an existing crack is extended during equilibrium increments, called f_{tol} and f^{g}_{tol}, respectively, in ABAQUS/CAE. This is defined by an admissible range as $1 < f < 1 + f_{tol}/ f^{g}_{tol}$, where f represents the ratio of fracture strength to the maximum principal stress of the element (Dassault Systèmes Simulia [19]).

While it is commonly recommended to use a reduced f_{tol} value, as advised in [49], it is crucial to find suitable tolerance values balancing the trade-off between providing reliable analysis and keeping the computational time needed for simulations to an acceptable level. To investigate the influence of tolerance limits, we conducted a comprehensive study, considering two different levels outlined in Table A.1. The analysis ranges from stringent criteria, with both f_{tol} and f^{g}_{tol} set to 10^{-6} for both shapes, and finally, to more lenient criteria (i.e., f_{tol} and f^{g}_{tol} both equal to 10^{-5}).

Table A.1
Residual inclusion pressure for different the tolerance limits (f_{tol} and f^{g}_{tol}).

Shapes	Tolerance for additional crack [f_{tol}]	Tolerance for existing crack growth [f^{g}_{tol}]	Residual Inclusion Pressure [GPa]
4:1:1	10^{-6}	10^{-6}	0.8115
	10^{-5}	10^{-5}	0.8116
10:1:1	10^{-6}	10^{-6}	0.7591
	10^{-5}	10^{-5}	0.7591

Our studies highlight that using the stricter criterium leads to negligible changes in the solutions for the considered problems. Therefore, we identify $f_{tol} = f^{g}_{tol} = 10^{-5}$ as a reasonable choice for all analyses reported in the present work.

Effect of pseudo-time step size and viscosity coefficients

In our numerical sensitivity study, we specifically focused on the 10:1:1 shape due to its pronounced stress concentration at the inclusion tip, potentially leading to unstable brittle fractures and subsequent stiffness matrix degradation (as detailed in Section 2.2).

As outlined in Section 2.2, we introduced a numerical viscosity coefficient equal to 10^{-4} Pa·s to address convergence challenges. In Table A.2, we highlight that considering a viscosity coefficient equal to 10^{-4} Pa·s allows for larger pseudo-time steps (namely, from $5{\cdot}10^{-6}$ s to 10^{-5} s) without affecting results in terms of relevant quantities such as the residual inclusion pressure. Therefore, the usage of this approach resulted in a remarkable reduction in computational time, from 48 h to 29 h.

Table A.2
Effect of time increment on the residual inclusion pressure and execution time.

Time increment [s]	Viscosity coefficient [Pa·s]	Residual inclusion pressure [GPa]	Execution time [h]
10^{-5}	10^{-4}	0.7591	29.46
$5{\cdot}10^{-6}$		0.7591	48.48

Then, for the optimal pseudo-time increment equal to $5{\cdot}10^{-6}$, we varied the viscosity coefficient (namely, we set it equal to $5{\cdot}10^{-5}$ Pa·s and 10^{-4} Pa·s) as highlighted in Table A.3, leading to negligible variations in terms of residual pressure in the inclusion.

Table A.3
Effect of viscosity coefficient on residual inclusion pressure.

Viscosity coefficient [Pa·s]	Time increment [s]	Residual inclusion pressure [GPa]
10^{-4}	$5{\cdot}10^{-6}$	0.7591
$5{\cdot}10^{-5}$		0.7598

Figure A.1 illustrates the stabilization energy dissipation, that is the stabilization energy with respect to the total strain energy of the system, for various inclusion shapes, ranging from 4:1:1 to 10:1:1, using the actual mesh specified in the analyses detailed in Section 3.2. The parameters set for these simulations include a time increment of 10^{-5} seconds, a viscosity coefficient of 10^{-4} Pa·s, and equal tolerances for f_{tol} and f^{g}_{tol}, set to 10^{-5}. The stabilization energy always increases, while the strain energy may decrease. Therefore, Abaqus/Standard restricts the ratio of the incremental value of the stabilization energy to the incremental value of the strain energy for each increment to ensure that this value has not exceeded the accuracy tolerance, if the ratio of the total stabilization energy to the total strain energy exceeds the accuracy tolerance.

The default accuracy tolerance used by the adaptive automatic stabilization scheme is 0.05, that is a default tolerance suitable for most applications. In fact, we can observe that, for all the shapes, the stabilization energy remains within 5 % with respect to the total strain energy.

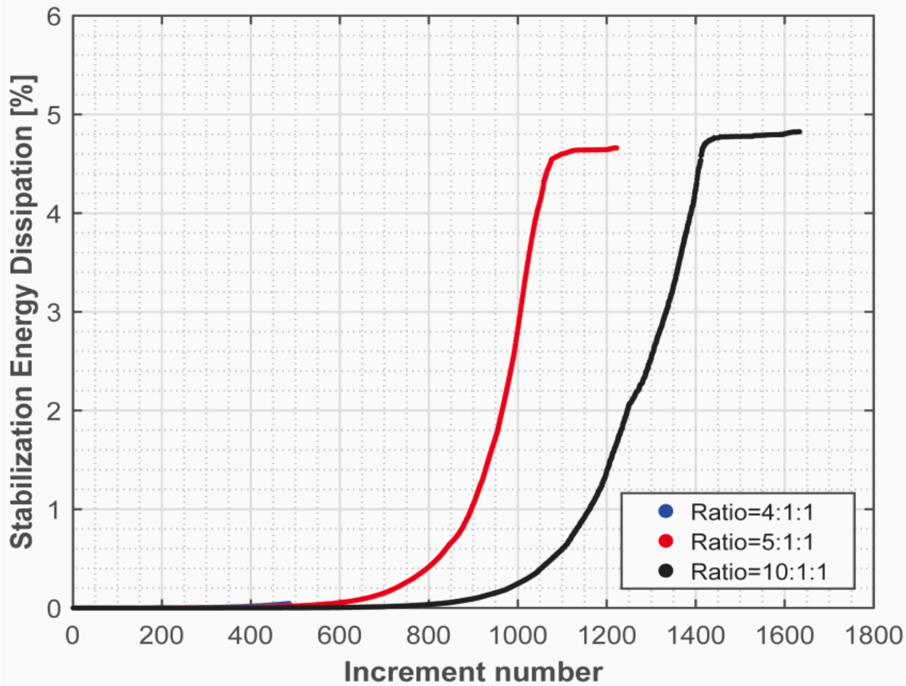

Fig. A.1. Stabilization energy dissipation versus increment number for different inclusion shapes (i.e., 4:1:1, 5:1:1, and 10:1:1). Throughout the simulation, the stabilization energy never exceeds 5 % of the total internal energy. Stabilization energy dissipation is the stabilization energy percentage with respect to the strain energy of the system. In this context, the increment number refers to the discrete calculation steps within a load step where the solver updates the system's state and ensures convergence before proceeding to the next increment.

Remark 2: Additional ABAQUS features in the modelling strategy

An efficient strategy for addressing issues of unstable crack growth involves allowing multiple elements at and ahead of a crack tip to fracture without imposing a substantial reduction in the increment size upon meeting the fracture criterion (Dassault Systèmes Simulia [19]. To facilitate this, the 'unstable crack growth' feature is activated in ABAQUS for all analyses. Additionally, we opted for ABAQUS's nodal smoothing feature. This technique effectively smoothens stress/strain fields ahead of the crack, contributing to enhanced result consistency.

Furthermore, the following keywords are used in all simulations:

Table A.4
ABAQUS keywords.

Keyword	Value/Setting
TOLERANCE	10^{-5}
GROWTH TOLERANCE	10^{-5}
Criterion	MAXPS
POSITION	NONLOCAL
SMOOTHING	NODAL
UNSTABLE GROWTH TOLERANCE	Not Applicable

Data availability

Data will be made available on request.

References

[1] Agrosì G, Nestola F, Tempesta G, Bruno M, Scandale E, Harris J. X-ray topographic study of a diamond from Udachnaya: Implications for the genetic nature of inclusions. *Lithos* 2016;248–251:153–9. https://doi.org/10.1016/j.lithos.2016.01.028.

[2] Agrosì G, Tempesta G, Della Ventura G, Cestelli Guidi M, Hutchison M, Nimis P, et al. Non-Destructive In Situ Study of Plastic Deformations in Diamonds: X-ray Diffraction Topography and μFTIR Mapping of Two Super Deep Diamond Crystals from São Luiz (Juina. Brazil) *Crystals* 2017;7(8):Article 8. https://doi.org/10.3390/cryst7080233.

[3] Alfano G, Crisfield MA. Finite element interface models for the delamination analysis of laminated composites: Mechanical and computational issues. *Int J Numer Meth Engng* 2001;50(7):1701–36. https://doi.org/10.1002/nme.93.

[4] Anderson, T. L. (2017). *Fracture Mechanics: Fundamentals and Applications, Fourth Edition* (4th ed.). CRC Press. https://doi.org/10.1201/9781315370293.

[5] Angel RJ, Alvaro M, Nestola F. 40 years of mineral elasticity: A critical review and a new parameterisation of equations of state for mantle olivines and diamond inclusions. *Phys Chem Miner* 2018;45(2):95–113. https://doi.org/10.1007/s00269-017-0900-7.

[6] Angel RJ, Alvaro M, Nestola F. Crystallographic Methods for Non-destructive Characterization of Mineral Inclusions in Diamonds. *Rev Mineral Geochem* 2022;88 (1):257–305. https://doi.org/10.2138/rmg.2022.88.05.

[7] Angel RJ, Mazzucchelli ML, Alvaro M, Nestola F. EosFit-Pinc: A simple GUI for host-inclusion elastic thermobarometry. *Am Mineral* 2017;102(9):1957–60. https://doi.org/10.2138/am-2017-6190.

[8] Angel, R. J., Mazzucchelli, M. L., Alvaro, M., & Nestola, F. (2020). "EosFit-Pinc: A simple GUI for host-inclusion elastic thermobarometry"—Reply to Zhong et al. *American Mineralogist*, *105*(10), 1587–1588. https://doi.org/10.2138/am-2020-7616CCBY.

[9] Angel RJ, Mazzucchelli ML, Alvaro M, Nimis P, Nestola F. Geobarometry from host-inclusion systems: The role of elastic relaxation. *Am Mineral* 2014;99(10): 2146–9. https://doi.org/10.2138/am-2014-5047.

[10] Angel RJ, Mazzucchelli ML, Musiyachenko KA, Nestola F, Alvaro M. Elasticity of mixtures and implications for piezobarometry of mixed-phase inclusions. *Eur J Mineral* 2023;35(4):461–78. https://doi.org/10.5194/ejm-35-461-2023.

[11] Anzolini C. Depth of formation of super-deep diamonds. *Plinius* 2018;44:1–7. https://doi.org/10.19276/plinius.2018.01001.

[12] Anzolini C, Angel RJ, Merlini M, Derzsi M, Tokár K, Milani S, et al. Depth of formation of CaSiO3-walstromite included in super-deep diamonds. *Lithos* 2016;265: 138–47. https://doi.org/10.1016/j.lithos.2016.09.025.

[13] Anzolini C, Nestola F, Mazzucchelli ML, Alvaro M, Nimis P, Gianese A, et al. Depth of diamond formation obtained from single periclase inclusions. *Geology* 2019;47(3):219–22. https://doi.org/10.1130/G45605.1.

[14] Barenblatt GI. The Mathematical Theory of Equilibrium Cracks in Brittle Fracture. In: Dryden HL, von Kármán Th, Kuerti G, van den Dungen FH, Howarth L, editors. *Advances in Applied Mechanics*, Vol. 7. Elsevier; 1962. p. 55–129. https://doi.org/10.1016/S0065-2156(08)70121-2.

[15] Camacho GT, Ortiz M. Computational modelling of impact damage in brittle materials. *Int J Solids Struct* 1996;33(20):2899–938. https://doi.org/10.1016/0020-7683(95)00255-3.

[16] Campione M, Malaspina N, Frezzotti ML. Threshold size for fluid inclusion decrepitation. *J Geophys Res Solid Earth* 2015;120(11):7396–402. https://doi.org/10.1002/2015JB012086.

[17] Campomenosi N, Angel RJ, Alvaro M, Mihailova B. Resetting of zircon inclusions in garnet: Implications for elastic thermobarometry. *Geology* 2023;51(1):23–7. https://doi.org/10.1130/G50431.1.

[18] Cohen LH, Rosenfeld JL. Diamond: Depth of Crystallization Inferred from Compressed Included Garnet. *J Geol* 1979;87(3):333–40. https://doi.org/10.1086/628422.

[19] Dassault Systèmes Simulia Corp. (2012). *Abaqus/CAE User's Manual (Version 6.12)*.

[20] Duarte APC, Díaz Sáez A, Silvestre N. Comparative study between XFEM and Hashin damage criterion applied to failure of composites. *Thin-Walled Struct* 2017; 115:277–88. https://doi.org/10.1016/j.tws.2017.02.020.

[21] Eshelby, J. (1957). The determination of the elastic field of an ellipsoidal inclusion, and related problems. *Proceedings of the Royal Society of London A: Mathematical, Physical and Engineering Sciences*, *241*, 376–396. https://doi.org/10.1098/rspa.1957.0133.

[22] Field JE, Pickles CSJ. Strength, fracture and friction properties of diamond. *Diam Relat Mater* 1996;5(6–8):625–34. https://doi.org/10.1016/0925-9635(95)00362-2.

[23] Foroozmehr F, Verreman Y, Chen J, Thibault D, Bocher P. Effect of inclusions on fracture behavior of cast and wrought 13% Cr-4% Ni martensitic stainless steels. *Engng Fract Mech* 2017;175:262–78. https://doi.org/10.1016/j.engfracmech.2017.02.002.

[24] Grassl P, Jirásek M, Gallipoli D. Initiation of fluid-induced fracture in a thick-walled hollow permeable sphere. *Eur J Mech A Solids* 2019;76:123–34. https://doi.org/10.1016/j.euromechsol.2019.04.004.

[25] Guiraud M, Powell R. P–V–T relationships and mineral equilibria in inclusions in minerals. *Earth Planet Sci Lett* 2006;244(3–4):683–94. https://doi.org/10.1016/j.epsl.2006.02.021.

[26] Harris, J. W., Milledge, H. J., Barron, T. H. K., & Munn, R. W. (1970). Thermal expansion of garnets included in diamond. *Journal of Geophysical Research (1896-1977)*, *75*(29), 5775–5792. https://doi.org/10.1029/JB075i029p05775.

[27] Hess P. The mechanical properties of various chemical vapor deposition diamond structures compared to the ideal single crystal. *J Appl Phys* 2012;111(5): 051101. https://doi.org/10.1063/1.3683544.

[28] Howell D, Nasdala L. Using strain birefringence in diamond to estimate the remnant pressure on an inclusion. *Aust J Earth Sci* 2008;55(8):1175–80. https://doi.org/10.1080/08120090802266709.

[29] Howell D, Wood IG, Dobson DP, Jones AP, Nasdala L, Harris JW. Quantifying strain birefringence halos around inclusions in diamond. *Contrib Miner Petrol* 2010; 160(5):705–17. https://doi.org/10.1007/s00410-010-0503-5.

[30] Izraeli ES, Harris JW, Navon O. Raman barometry of diamond formation. *Earth Planet Sci Lett* 1999;173(3):351–60. https://doi.org/10.1016/S0012-821X(99)00235-6.

[31] Kohn MJ, Mazzucchelli ML, Alvaro M. Elastic Thermobarometry. *Annu Rev Earth Planet Sci* 2023;51(1):331–66. https://doi.org/10.1146/annurev-earth-031621-112720.

[32] Kueter N, Soesilo J, Fedortchouk Y, Nestola F, Belluco L, Troch J, et al. Tracing the depositional history of Kalimantan diamonds by zircon provenance and diamond morphology studies. *Lithos* 2016;265:159–76. https://doi.org/10.1016/j.lithos.2016.05.003.

[33] Lacazette A. Application of linear elastic fracture mechanics to the quantitative evaluation of fluid-inclusion decrepitation. *Geology* 1990;18(8):782–5. https://doi.org/10.1130/0091-7613(1990)018<0782:AOLEFM>2.3.CO;2.

[34] Langenfeld K, Kurzeja P, Mosler J. How regularization concepts interfere with (quasi-)brittle damage: A comparison based on a unified variational framework. *Contin Mech Thermodyn* 2022;34(6):1517–44. https://doi.org/10.1007/s00161-022-01143-2.

[35] Liang Q, Yan C, Meng Y, Lai J, Krasnicki S, Mao H, et al. Recent advances in high-growth rate single-crystal CVD diamond. *Diam Relat Mater* 2009;18(5): 698–703. https://doi.org/10.1016/j.diamond.2008.12.002.

[36] Luisier C, Tajčmanová L, Yamato P, Duretz T. Garnet microstructures suggest ultra-fast decompression of ultrahigh-pressure rocks. *Nat Commun* 2023;14(1): 6012. https://doi.org/10.1038/s41467-023-41310-w.

[37] Mazzucchelli ML, Angel RJ, Rustioni G, Milani S, Nimis P, Domeneghetti MC, et al. Elastic geobarometry and the role of brittle failure on pressure release. *Geophys Res Abstr* 2016;18:13569.

[38] Mazzucchelli ML, Burnley P, Angel RJ, Morganti S, Domeneghetti MCC, Nestola F, et al. Elastic geothermobarometry: Corrections for the geometry of the host-inclusion system. *Geology* 2018;46(3):231–4. https://doi.org/10.1130/G39807.1.

[39] Mazzucchelli ML, Reali A, Morganti S, Angel RJ, Alvaro M. Elastic geobarometry for anisotropic inclusions in cubic hosts. *Lithos* 2019;105218. https://doi.org/10.1016/j.lithos.2019.105218.

[40] Melenk JM, Babuška I. The partition of unity finite element method: Basic theory and applications. *Comput Methods Appl Mech Engng* 1996;139(1):289–314. https://doi.org/10.1016/S0045-7825(96)01087-0.

[41] Moës N, Dolbow J, Belytschko T. A finite element method for crack growth without remeshing. *Int J Numer Meth Engng* 1999;46(1):131–50. https://doi.org/10.1002/(SICI)1097-0207(19990910)46:1<131::AID-NME726>3.0.CO;2-J.

[42] Morganti S, Mazzucchelli ML, Alvaro M, Reali A. A numerical application of the Eshelby theory for geobarometry of non-ideal host-inclusion systems. *Meccanica* 2020;1–14. https://doi.org/10.1007/s11012-020-01135-z.

[43] Moulas E, Podladchikov Y, Zingerman K, Vershinin A, Levin V. Large-strain Elastic and Elasto-Plastic Formulations for Host-Inclusion Systems and Their Applications in Thermobarometry and Geodynamics. *Am J Sci* 2023;323. https://doi.org/10.2475/001c.68195.

[44] Murri M, Mazzucchelli ML, Campomenosi N, Korsakov AV, Prencipe M, Mihailova BD, et al. Raman elastic geobarometry for anisotropic mineral inclusions. *Am Mineral* 2018;103(11):1869–72. https://doi.org/10.2138/am-2018-6625CCBY.
[45] Nestola F, Korolev N, Kopylova M, Rotiroti N, Pearson DG, Pamato MG, et al. CaSiO3 perovskite in diamond indicates the recycling of oceanic crust into the lower mantle. *Nature* 2018;555(7695):237–41. https://doi.org/10.1038/nature25972.
[46] Nestola F, Nimis P, Ziberna L, Longo M, Marzoli A, Harris JW, et al. First crystal-structure determination of olivine in diamond: Composition and implications for provenance in the Earth's mantle. *Earth Planet Sci Lett* 2011;305(1):249–55. https://doi.org/10.1016/j.epsl.2011.03.007.
[47] Nestola F, Zaffiro G, Mazzucchelli ML, Nimis P, Andreozzi GB, Periotto B, et al. Diamond-inclusion system recording old deep lithosphere conditions at Udachnaya (Siberia). *Sci Rep* 2019;9(1):12586. https://doi.org/10.1038/s41598-019-48778-x.
[48] Nimis P, Alvaro M, Nestola F, Angel RJ, Marquardt K, Rustioni G, et al. First evidence of hydrous silicic fluid films around solid inclusions in gem-quality diamonds. *Lithos* 2016;260:384–9. https://doi.org/10.1016/j.lithos.2016.05.019.
[49] Nuclear Regulatory Commission. (2020, August 21). Benchmarks and sensitivity studies for subcritical crack growth analyses using XFEM in Abaqus/Standard. https://www.nrc.gov/docs/ML2025/ML20253A154.pdf.
[50] Oh Y-J, Lee B-S, Hong J-H. The effect of non-metallic inclusions on the fracture toughness master curve in high copper reactor pressure vessel welds. *J Nucl Mater* 2002;301(2):108–17. https://doi.org/10.1016/S0022-3115(02)00716-X.
[51] Pearson DG, Brenker FE, Nestola F, McNeill J, Nasdala L, Hutchison MT, et al. Hydrous mantle transition zone indicated by ringwoodite included within diamond. *Nature* 2014;507(7491):221–4. https://doi.org/10.1038/nature13080.
[52] Rustioni G. *Pressure release for host–inclusion systems: The interplay between brittle failure and fluid phase* [M.Sc. Thesis]. University of Pavia; 2016.
[53] Rustioni, G., Angel, R., Mazzucchelli, M., Milani, S., Nimis, P., Domeneghetti, M., Marone, F., Harris, J., Nestola, F., & Alvaro, M. (2016). *Pressure release for host - inclusion systems: The interplay between brittle failure and fluid phase*. EMC 2016 - 2nd European Mineralogical Congress. https://scholar.google.com/scholar?hl=en&as_sdt=0%2C5&q=Pressure+release+for+host+-+inclusion+systems%3A+The+interplay+between+brittle+failure+and+fluid+phase&btnG=.
[54] Rustioni G, Angel R, Milani S, Mazzucchelli M, Nimis P, Domeneghetti M, et al. Elastic geobarometry for host-inclusion systems: Pressure release and the role of brittle failure. *Rendiconti Online Della Società Geologica Italiana* 2015;35:137.
[55] Shirey SB, Cartigny P, Frost DJ, Keshav S, Nestola F, Nimis P, et al. Diamonds and the Geology of Mantle Carbon. *Rev Mineral Geochem* 2013;75(1):355–421. https://doi.org/10.2138/rmg.2013.75.12.
[56] Sobolev NV, Fursenko BA, Goryainov SV, Shu J, Hemley RJ, Mao H, et al. Fossilized high pressure from the Earth's deep interior: The coesite-in-diamond barometer. *Proc Natl Acad Sci* 2000;97(22):11875–9. https://doi.org/10.1073/pnas.220408697.
[57] Srivastava A, Ponson L, Osovski S, Bouchaud E, Tvergaard V, Needleman A. Effect of inclusion density on ductile fracture toughness and roughness. *J Mech Phys Solids* 2014;63:62–79. https://doi.org/10.1016/j.jmps.2013.10.003.
[58] Tanné E, Li T, Bourdin B, Marigo J-J, Maurini C. Crack nucleation in variational phase-field models of brittle fracture. *J Mech Phys Solids* 2018;110:80–99. https://doi.org/10.1016/j.jmps.2017.09.006.
[59] Unger JF, Eckardt S, Könke C. Modelling of cohesive crack growth in concrete structures with the extended finite element method. *Comput Methods Appl Mech Engng* 2007;196(41):4087–100. https://doi.org/10.1016/j.cma.2007.03.023.
[60] Voigt W. Lehrbuch der Kristallphysik. In Kristalloptik: Teubner; 1910.
[61] Wang Y, Nestola F, Li H, Hou Z, Pamato MG, Novella D, et al. In situ single-crystal X-ray diffraction of olivine inclusion in diamond from Shandong, China: Implications for the depth of diamond formation. *Eur J Mineral* 2023;35(3):361–72. https://doi.org/10.5194/ejm-35-361-2023.
[62] Wells GN, Sluys LJ. A new method for modelling cohesive cracks using finite elements. *Int J Numer Meth Engng* 2001;50(12):2667–82. https://doi.org/10.1002/nme.143.
[63] Wenz MD, Jacobsen SD, Zhang D, Regier M, Bausch HJ, Dera PK, et al. Fast identification of mineral inclusions in diamond at GSECARS using synchrotron X-ray microtomography, radiography and diffraction. *J Synchrotron Radiat* 2019;26(5):1763–8. https://doi.org/10.1107/S1600577519006854.
[64] Whitney DL, Cooke ML, Du Frane SA. Modeling of radial microcracks at corners of inclusions in garnet using fracture mechanics. *J Geophys Res Solid Earth* 2000;105(B2):2843–53. https://doi.org/10.1029/1999JB900375.
[65] Wu J-Y, Qiu J-F, Nguyen VP, Mandal TK, Zhuang L-J. Computational modeling of localized failure in solids: XFEM vs PF-CZM. *Comput Methods Appl Mech Engng* 2019;345:618–43. https://doi.org/10.1016/j.cma.2018.10.044.
[66] Zhang Y. Mechanical and phase equilibria in inclusion-host systems. *Earth Planet Sci Lett* 1998;157(3–4):209–22. https://doi.org/10.1016/S0012-821X(98)00036-3.
[67] Zhang Y, Sun H, Chen C. Atomistic Deformation Modes in Strong Covalent Solids. *Phys Rev Lett* 2005;94(14):145505. https://doi.org/10.1103/PhysRevLett.94.145505.
[68] Zhong X, Andersen NH, Dabrowski M, Jamtveit B. Zircon and quartz inclusions in garnet used for complementary Raman thermobarometry: Application to the Holsnøy eclogite, Bergen Arcs, Western Norway. *Contrib Miner Petrol* 2019;174(6):50. https://doi.org/10.1007/s00410-019-1584-4.
[69] Zhong X, Dabrowski M, Jamtveit B. Analytical solution for residual stress and strain preserved in anisotropic inclusion entrapped in an isotropic host. *Solid Earth* 2021;12(4):817–33. https://doi.org/10.5194/se-12-817-2021.
[70] Zhong X, Moulas E, Tajčmanová L. Tiny timekeepers witnessing high-rate exhumation processes. *Sci Rep* 2018;8(1):Article 1. https://doi.org/10.1038/s41598-018-20291-7.
[71] Zhong X, Wallis D, Kingsbery P, John T. The effect of aqueous fluid on viscous relaxation of garnet and modification of inclusion pressures after entrapment. *Earth Planet Sci Lett* 2024;636:118713. https://doi.org/10.1016/j.epsl.2024.118713.
[72] Zhu Y, Lu Y-M, Huang C-W, Liang Y-L. The effect of TiN inclusions on the fracture mechanism of 20CrMnTi steel with lath martensite. *Mater Res Express* 2020;7(3):036509. https://doi.org/10.1088/2053-1591/ab7ac3.
[73] Howell D, Piazolo S, Dobson DP, Wood IG, Jones AP, Walte N, Frost DJ, Fisher D, Griffin WL. Quantitative characterization of plastic deformation of single diamond crystals: A high pressure high temperature (HPHT) experimental deformation study combined with electron backscatter diffraction (EBSD). Diamond Relat Mater 2012;30:20–30. https://doi.org/10.1016/j.diamond.2012.09.003.
[74] Angel RJ, Alvaro M, Nestola F, Mazzucchelli ML. Diamond thermoelastic properties and implications for determining the pressure of formation of diamond-inclusion systems. Russ Geol Geophys 2015;56(1):211–20. https://doi.org/10.1016/j.rgg.2015.01.014.